Journal of Materials Chemistry B

ROYAL SOCIETY OF CHEMISTRY

PAPER

Cite this: *J. Mater. Chem. B*, 2023, **11**, 1057

Synthesis and characterization of nano crystallite plaster of Paris prepared from waste eggshells and exploration of cytotoxicity, hemolysis and antimicrobial properties

Md. Sahadat Hossain, [a] Md. Najem Uddin, [b] Shirin Akter Jahan[a] and Samina Ahmed *[ab]

Received 2nd November 2022,
Accepted 25th December 2022

DOI: 10.1039/d2tb02392j

rsc.li/materials-b

Plaster of Paris, a well-known biomaterial, was synthesized from waste eggshells, which were chosen as an available bio-source of calcium. The produced plaster of Paris was characterized by X-ray diffraction (XRD), Fourier Transform Infrared (FTIR), Raman spectroscopy, UV-Vis spectroscopy, and SEM images along with a few crystallographic parameters such as crystallite size (Scherrer equation and different model equations), lattice parameters, crystallinity index, the volume of the unit cell, microstrain, dislocation density, growth preference, and residual stress from the XRD-$\sin^2\Psi$ technique. The biomedical competency of the prepared plaster of Paris was evaluated utilizing the cytotoxicity, hemolysis, and antimicrobial activity of *E. coli* and *S. aureus*. The cytotoxicity assessment has revealed that the percentages of viable cells were 93–98% and a highly hemocompatible nature (<5%) was exerted by the sample. The plaster of Paris only revealed antimicrobial properties against Gram-positive bacteria (*S. aureus*), and no effect was noticed for Gram-negative bacteria (*E. coli*).

Introduction

There is a long history of plaster of Paris being used in medical sectors but its application as a bandage was coined in the 1950s by two surgeons, namely Antonius Mathijsen and Nikolai Ivanovich Pirogov.[1,2] The ancient Greek, Egyptian, and Roman civilizations used plaster of Paris nearly 9000 years ago[3] and since then the application sectors have been increasing day by day, especially in the medical field. The wide applications include bone regeneration, drug delivery, dental prosthetics, heritage conservation, and construction.[4] As the applications and demand in the medical sectors for synthesized biomaterials are increasing day by day, researchers are looking for a sustainable and available source of biomaterials. Sustainability not only depends on the advanced properties of biomaterials but also on the continuous supply of raw materials. Plaster of Paris is a widely known biomaterial that has inherent biodegradable properties.[5] The hydration reaction is another important characteristic of bassanite where 1.5 moles of H_2O are attached to form gypsum, which shows lower solubility in water (0.24 g in 100 ml).[6] It has been predicted that nearly 5–10% of all orthopedic-relevant patients with long bone problems face delayed union or lead to a nonunion.[7] In such a case, plaster of Paris is one of the best choices. A few researchers have found complexity during the applications of calcium sulfate in biomedical applications (nearly 10%[8]). There are various types of complexity associated with applications of foreign biomaterials in the human body, either during the presence of the biomaterial inside the body or in contact with the body.[9,10] The concern related to the interaction between the applied materials and the immune system is another major issue in biomaterial applications.[11] To minimize such problems, a bio-origin of the biomaterials can be a good choice for safe application. Calcium sulfate-based compounds are found in nature as gypsum ($CaSO_4{\cdot}2H_2O$) and anhydrite ($CaSO_4$), which further can be converted to plaster of Paris. Generally, the top most synthesized inorganic compound, basanite, is produced from the dehydration of gypsum at the temperature range of 100 to 150 °C.[12] To minimize the dependency on the stored natural sources, relevant research studies to find alternative sources are ongoing. In tune with this, calcium-containing eggshells were chosen as the source of calcium for the alternative production of bassanite. And, the waste source of raw materials adds extra benefit to utilizing waste materials for valuable biomaterials. There is a research gap related to these two advantages of the utilization of waste materials and bio-origin. Eggshells are a widely known

[a] *Institute of Glass & Ceramic Research and Testing, Bangladesh Council of Scientific and Industrial Research (BCSIR), Dhaka-1205, Bangladesh. E-mail: shanta_samina@yahoo.com*
[b] *BCSIR Laboratories Dhaka, Bangladesh Council of Scientific and Industrial Research (BCSIR), Dhaka-1205, Bangladesh*

bioresource, which are composed of mainly calcite phase of calcium carbonate, roughly 95%.[13] Around the globe, nearly 250 000 tons of eggshells are produced which are going to be a burden for a sustainable environment. This waste is utilized in a number of ways as a rich source of calcium carbonate. Different types of biomaterials are synthesized from the waste eggshells such as hydroxyapatite,[14] Mg and Zr composite reinforced with eggshells,[15] calcium oxide, calcium carbonate, calcium hydroxide, calcium-deficient hydroxyapatite, tricalcium phosphate, tetracalcium phosphate,[16] *etc.* To meet the sustainability requirements of plaster of Paris, waste eggshells were chosen as a low cost raw source of calcium.

In this research, waste eggshells were utilized to synthesize plaster of Paris (calcium sulfate hemihydrate), which was further assessed for application as a biomaterial. The crystallographic characterization was also explored by engaging the X-ray diffraction technique.

Materials

Waste eggshells were collected from a nearby market of the Bangladesh Council of Scientific and Industrial Research (BCSIR), Dhaka, Bangladesh, and the quantification of the calcium percentage was performed utilizing an XRF (X-ray fluorescence) machine. Analytical Grade Sulfuric acid was purchased from E-Merck Germany and the DI (deionized water) was prepared in the Glass Research Division Laboratory of BCSIR.

Plaster of Paris synthesis

Before use, the eggshells were cleaned with DI water at 90 °C for 4 h with subsequent ball milling for preparation of a powder. From the powdered eggshells, a 1 M suspension was prepared in 100 ml and the same volume with the same molarity of sulfuric acid was prepared. The acid was dropwise added from a burette into the calcium carbonate suspension. The precipitate of calcium sulfate was kept under stirring for 24 h at normal room temperature. The following day, after filtering, the synthesized sample was dried in a vacuum oven at 50 °C for 6 h. The sample was kept in a polyethylene bag until further testing. To get the desired plaster of Paris, the synthesized sample was heated at 200 °C for 120 min. The chemical reactions for the synthesis of the plaster of Paris are revealed in eqn (1)–(3).

$$\text{Waste Eggshells} + H_2O \rightarrow CaCO_3\text{-suspension} \quad (1)$$

$$CaCO_3\ (\text{suspension}) + 98\%\ H_2SO_4 \rightarrow CaSO_4{\cdot}2H_2O \quad (2)$$

$$CaSo_4 \cdot 2H_2O \xrightarrow{\text{Heating at } 200\ ^\circ\text{C, } 2\text{ h}} CaSo_4 \cdot 0.5H_2O\ (\text{Plaster of Paris}) \quad (3)$$

X-ray diffraction analysis

Crystallographic characterization of the synthesized plaster of Paris was executed with the help of a Rigaku Smart Lab XRD machine. The data were registered in the 2θ range of 5–80 degrees maintaining steps of 0.01. Before performing the sample analysis, the machine was calibrated using the standard silicon reference. The machine was operated at 23 °C temperature fixing the flow rate of 4.6–4.8 L min^{-1}. Copper was used as the source of X-rays (CuKα, λ = 1.54060 Å), which was made of ceramic and operated at 40 kV and 50 mA. The data collection mode was Bragg–Brentano parafocusing geometry and the Kβ ray of copper was filtered out using a Ni-filter which was placed before the detector. The produced pattern was matched with the standard ICDD database from pdf + 4 2022.

FTIR analysis

An IR-Prestige 21 machine (Shimadzu, Japan) machine was utilized to identify the functional groups in the synthesized sample, which was operated by attaching an attenuated total reflectance (ATR). The machine collected data in the range of 400 to 4000 cm^{-1} wavenumber on a percentage transmittance basis. The final accumulated data were obtained from an average of 30 scans maintaining 4 cm^{-1} spectral resolution.

Raman spectroscopy

Raman spectroscopic analysis was performed to evaluate the Raman active groups in the synthesized sample engaging a high-resolution HORIBA MacroRAMTM spectrometer. The operating conditions of the machine were a wavelength of 785 nm, 7–450 mW power, focal length of 115 mm, and a spectrum range of 100–3500 cm^{-1}.

UV-Vis spectrophotometer

The optical bandgap of the synthesized plaster of Paris was measured by engaging a UV-Vis-spectrophotometer (Shimadzu, Japan, model: U-2900). The experiment was carried out at the normal room temperature (25 °C) and relative humidity of more than 60%.

Hemolysis test

The application of any material in the human body depends on a number of characteristics and hemolysis is one of the most important, which identifies the ability of materials to breakdown human red blood cells (RBCs). The hemolysis assessment of the synthesized plaster of Paris was performed according to a well-established methodology where heparin (Country: China, Pharmaceutical Grade) was chosen as an anti-coagulant agent during the collection of blood.[17,18] Water was taken as a positive control and physiological saline extract solution (Country: China, Pharmaceutical Grade) was chosen as a negative control. An exact 0.2 ml blood sample was taken and subsequently diluted and then incubated for 60 min at 37 °C. Different amounts of sample such as 50, 100, and 200 μg ml^{-1} were taken, and kept for 2 h. After that, the solution was centrifuged for 5 min at 3000 rpm and then the absorbance, mainly at 545 nm, was taken using a UV-Vis spectrophotometer. The percentage of hemolysis (H_p) was measured following eqn (4).[19,20]

Hemolysis (%),

$$H_p = \frac{A_{sample} - A_{negative\ control}}{A_{positive\ control} - A_{negative\ control}} \times 100 \quad (4)$$

where, A_{sample}, $A_{negative\ control}$, and $A_{positive\ control}$ are the mean absorbance at 545 nm of the sample, negative control and positive control, respectively.

Cytotoxicity assessment

The Trypan Blue Exclusion method was engaged to estimate the viable and non-viable cells for the assessment of the synthesized plaster of Paris as a biomaterial. Vero cells (CLS 605372, Germany) of the Kidneys from the African Green Monkey were interacted with the plaster of Paris to assay the cytotoxic effect of the biomaterial and the test methodology was documented in published articles.[21] Various doses of sample, such as 50, 100, and 200 μg ml^{-1} were taken for steam sterilization and then interacted with the cells. After 72 h the viable and non-viable cells were counted with the assistance of an automated cell counter (LUNA-II™, Analytikjena) following the Trypan Blue Exclusion method. The percentage of viable cells was computed using eqn (5).[21,22]

$$\text{Percentage of viable cells} = \frac{\text{Number of viable cells}}{\text{Total number of cells}} \times 100 \quad (5)$$

Antimicrobial activity test

The agar well diffusion method was engaged to evaluate the antimicrobial activity of the synthesized product for a Gram-positive bacteria *Staphylococcus aureus* (ATCC-9144) (*S. aureus*), and a Gram-negative bacteria *Escherichia coli* (ATCC-11303) (*E. coli*). The details of the method are documented in a number of literature studis.[23,24] Fresh cultures of each bacterium with 0.5 McFarland standard turbidity were spread uniformly on the surface of nutrient agar media. The well was formed with 6 mm diameter using a sterile cork borer. To estimate the antimicrobial effect, 50 μl of 200 μg ml^{-1} concentration of sample was added in each well. DMSO (%5) (E-Merck Germany) was prepared as a negative control and a kanamycin (30 μg) (Country: China, Pharmaceutical Grade) disk was used as a positive control. The plate was kept for 3 h at 4 °C to ensure diffusion before incubation at 37 °C for 24 h. After the incubation period, the diameter of the inhibition zone was measured.

Statistical analysis

A one-way Analysis of Variance (ANOVA) test was executed to associate the obtained data of plaster of Paris and the value $p < 0.05$ was chosen as statistically significant and $p > 0.05$ was taken as statistically non-significant.[25] The statistical analysis was performed engaging Origin Pro software and the procedure is explained elsewhere.[26]

Results and discussion

Phase and crystallographic analysis

The crystallographic characterization of the plaster of Paris was explored by engaging X-ray diffraction and the originated pattern is revealed here in Fig. 1. The synthesized product was characterized as plaster of Paris by comparing the XRD pattern with the standard ICDD database of card no: #00-041-0224. The originated peaks for the synthesized product were 14.82(200), 25.73(020), 29.80(400), 31.94(204), 33.06(402), 38.50(024), 42.35(422), 49.39(−424), 54.17(604), 63.11(244), 70.00(640), 72.69(428), and 76.71(338). A similar type of diffraction pattern was reported for the pure bassanite phase.[27] A number of crystallographic parameters including crystallite size, lattice parameters, crystallinity index, volume of unit cell, microstrain, and dislocation density were investigated for the comprehensive understanding of the material properties. The crystallite size was measured engaging the Scherrer equation as presented in eqn (6).[11] The mentioned parameters for plaster of Paris of monoclinic crystal and *I*2(5) space group were computed utilizing eqn (6)–(10) and the details of these equations are documented in the published articles.[28–30]

Crystallite size,

$$D_c = \frac{K\lambda}{\text{FWHM}\cos\theta} \quad (6)$$

Lattice parameter equation (monoclinic),

$$\frac{1}{d^2} = \frac{1}{\sin^2\beta}\left(\frac{h^2}{a^2} + \frac{k^2\sin^2\beta}{b^2} + \frac{l^2}{c^2} - \frac{2hl\cos\beta}{ac}\right) \quad (7)$$

Dislocation density,

$$\delta = \frac{1}{(D_c)^2} \quad (8)$$

Microstrain,

$$\varepsilon = \frac{\beta}{4\tan\theta} \quad (9)$$

Crystallinity index,

$$CI = \frac{H_{200} + H_{020} + H_{400}}{H_{400}} \quad (10)$$

In the overhead equation, FWHM = full width at half maxima in radian; the constant of the Scherrer's equation, K = 0.94; λ = wavelength of X-ray source = 0.15406 nm;

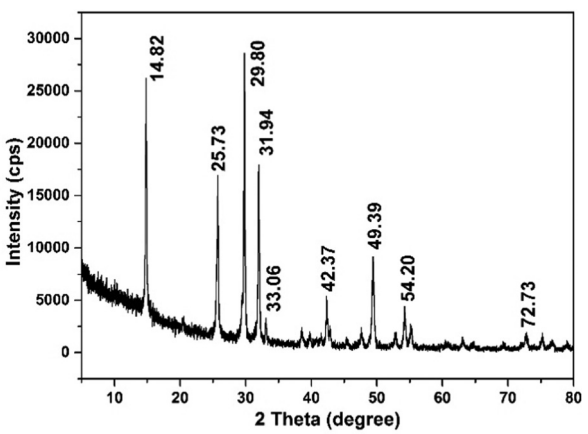

Fig. 1 X-ray diffraction pattern of bassanite synthesized from eggshell.

θ = diffraction angle; a, b, c, and h, k, l = lattice parameters of the crystals; H_{hkl} = peak height of the respective plane for the three strongest peaks.

Eqn (6), the Scherrer's equation expresses the crystallite of materials and the calculated crystallite size of the synthesized plaster of Paris was 46 nm. The computed lattice parameters from eqn (5) were a = 11.94 Å, b = 6.92 Å, c = 12.65 Å, which were very close to the standard values of ICDD Card no: #00-041-0224: a = 12.02 Å, b = 6.932 Å, c = 12.691 Å. The dislocation density, microstrain and crystallinity index were measured engaging eqn (7)–(10) and the values were 0.47 line per m^2, 0.33, and 2.33, respectively.

As the plaster of Paris was synthesized from waste eggshells, the growth preference of the crystals depends on the reaction parameters. The direction of growth is expressed by the plane preference of the crystal, which can be estimated from the relative intensities of the sample by comparing the intensities of the standard. The relative intensity (RI) of a specific plane, here (200), can be calculated from eqn (11).[31]

Relative intensity,

$$\mathrm{RI}_{\mathrm{plaster}} = \frac{I_{(200)}}{I_{(020)} + I_{(204)} + I_{(400)}} \quad (11)$$

The measured relative intensities from eqn (8) of the (200) plane for the synthesized plaster of Paris and standard were 0.39 and 0.33, respectively. The growth preference of the (200) plane was measured using the relative intensities of the sample and standard following eqn (12).[28]

Growth preference,

$$P = \frac{\mathrm{RI}_{\mathrm{plaster}} - \mathrm{RI}_{\mathrm{standard}}}{\mathrm{RI}_{\mathrm{standard}}} \quad (12)$$

The computed growth preference for the plaster of Paris was 0.182 and following the same procedure the growth preference of the characteristic peaks can be estimated. The positive value of the growth preference of the (200) plane indicated the thermodynamically stable plane in the reaction conditions.

The calculated crystallite size from the Scherrer equation and the density (ρ) of the standard sample (ICDD database) were taken into consideration for the measurement of the specific surface area following eqn (13). A detailed explanation of the equation can be found in the literature.[32,33] The calculated specific surface area of the plaster of Paris was 48 m^2 g^{-1}.

Specific surface area,

$$S = \frac{6 \times 10^3}{\rho \times D_{\mathrm{c}}} \quad (13)$$

Calculation of crystallite size using various models

Sahadat–Scherrer model

To estimate the crystallite size properly a number of model equations were utilized and for more precise data the Sahadat–Scherrer model was utilized, which can be mathematically expressed as eqn (14).[34] This model was based on the Scherrer equation and modified to generate a straight line passing through the origin. To construct a straight line, $\cos\theta$ was taken on the y-axis and $\frac{1}{\mathrm{FWHM}}$ was placed on the x-axis and then another line was built which passed through the origin utilizing Microsoft excel. The built equation $y = 0.0028x$ was compared with eqn (14) and the crystallite size was calculated from the slope. The pictorial view of the Sahadat–Scherrer model is revealed here in Fig. 2 with an inscribed crystallite size of 49 nm.

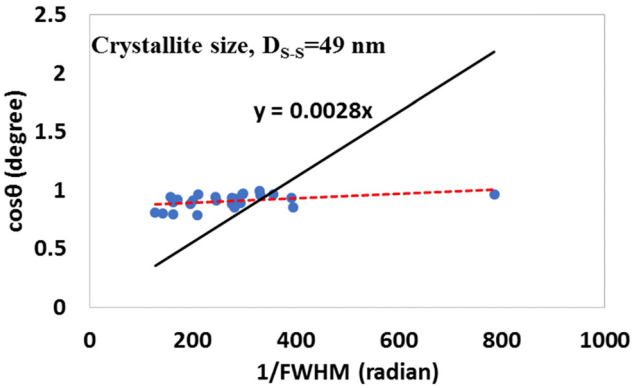

Fig. 2 Crystallite size of plaster of Paris engaging the Sahadat–Scherrer model.

Sahadat–Scherrer model,

$$\cos\theta = \frac{K\lambda}{D_{\mathrm{S-S}}} \times \frac{1}{\beta} \quad (14)$$

Linear straight-line method of Scherrer's equation

The linear straight-line method of Scherrer's equation is another widely used model for the prediction of the crystallite size of any crystalline material from powder diffraction data. The model can be expressed as eqn (15) and the explanation is documented in a number of literature reports.[35] Fig. 3 presents the corresponding graph with a crystallite size of 462 nm, but this model cannot be applicable for the synthesized plaster of Paris.

Linear straight-line model,

$$\cos\theta = \frac{K\lambda}{D_{\mathrm{c}}} \times \frac{1}{\mathrm{FWHM}} = \frac{K\lambda}{D_{\mathrm{L}}} \times \frac{1}{\mathrm{FWHM}} \quad (15)$$

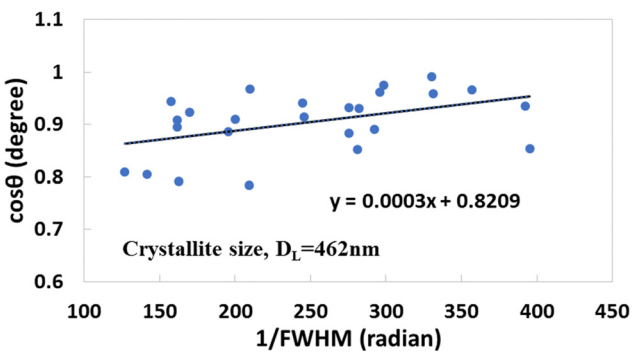

Fig. 3 Crystallite size of plaster of Paris using the linear straight-line method of Scherrer's equation.

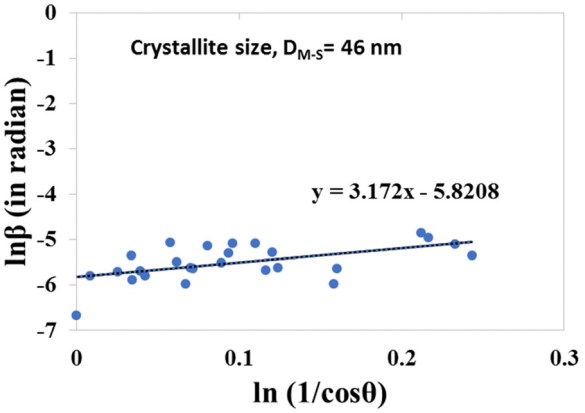

Fig. 4 Crystallite size of plaster of Paris calculated from the Monshi–Scherrer model.

Monshi–Scherrer model

A modified Scherrer model is also applicable to measure the crystallite size precisely, which is also based on the Scherrer model and mathematically this model can be presented as eqn (16) if the crystallite size is denoted as D_{M-S}.[36,37] When a straight line was built as presented in Fig. 4, the calculated crystallite size was 46 nm.

Monshi–Scherrer model,

$$\ln \beta = \ln \frac{1}{\cos \theta} + \ln \frac{K\lambda}{D_{M-S}} \quad (16)$$

Williamson–Hall plot

A Williamson–Hall plot, also known as a strain-induced model, was constructed by considering the instrumental broadening, intrinsic strain broadening and size broadening. The Williamson–Hall model can be represented as eqn (17)[36] where D_{W-H} and ε are the crystallite size and intrinsic strain, respectively. A straight line was formed as presented in Fig. 5 and the measured crystallite size was 60 nm.

Williamson–Hall plot,

$$\beta_{total} \cos \theta = \frac{K_B \lambda}{D_{W-H}} + 4\varepsilon \sin \theta \quad (17)$$

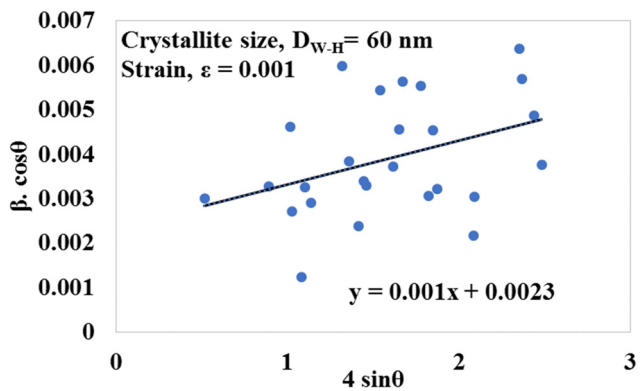

Fig. 5 Crystallite size and intrinsic strain of plaster of Paris utilizing the Williamson–Hall model.

The XRD-sin^2 Ψ technique for residual stress calculation

To measure the residual stress inside the crystalline materials the XRD-sin^2 Ψ technique, which is widely used in the case of polycrystalline materials, was operated for the synthesized plaster of Paris. The crystal defects such as dislocation, micro-strain, impurities, point defects, *etc.* are the influencing factors for the origination of intrinsic stress which deviated the lattice parameters from the standard. Eqn (18)–(21) were engaged to compute the residual stress and the details can be found in the literature.[35,38]

$$\frac{d_{\phi\Psi} - d_0}{d_0} = \frac{1+v}{E} \cdot \sigma_\phi \cdot \sin^2 \Psi - \frac{v}{E}(\sigma_1 + \sigma_2) \quad (18)$$

$$\frac{d_{\phi\Psi} - d_0}{d_0} = \frac{1+v}{E} \cdot \sigma \cdot \sin^2 \Psi - \frac{v}{E}(\sigma + \sigma) \quad (19)$$

Or,

$$\frac{d_{\phi\Psi} - d_0}{d_0} = \frac{1+v}{E} \cdot \sigma \cdot \sin^2 \Psi - \frac{2v}{E}\sigma \quad (20)$$

Or,

$$d_{\phi\Psi} = \left[\frac{1+v}{E} \cdot \sin^2 \Psi - \frac{2v}{E}\right]\sigma \cdot d_0 + d_0 \quad (21)$$

Here, d_0 is the stress-free d-spacing, $d_{\phi\Psi}$ is the d-spacing containing intrinsic stress, σ_ϕ is the stress in plane, σ_1 and σ_2 are the stress components, and Ψ is the tilt angle. The values of Young's modulus (E) and Poisson's ratio (v) were documented in the literature.[39–41] The formed graph is revealed here in Fig. 6 and the estimated residual stress was −371 GPa.

Functional groups analysis

The functional groups of the synthesized plaster of Paris were marked out with the aid of an FTIR machine and the sample inherited only two activating groups, namely sulphate and hydroxyl. The FTIR spectra of the synthesized plaster of Paris are revealed here in Fig. 7. At 594, 650, and 1089 cm^{-1} wavenumber, three strong peaks were visualized for the existence of sulphate groups. The presence of water molecules in the sample produced a strong peak at 3650 cm^{-1} wavenumber along with 1625 cm^{-1} wavenumber, which are characteristic

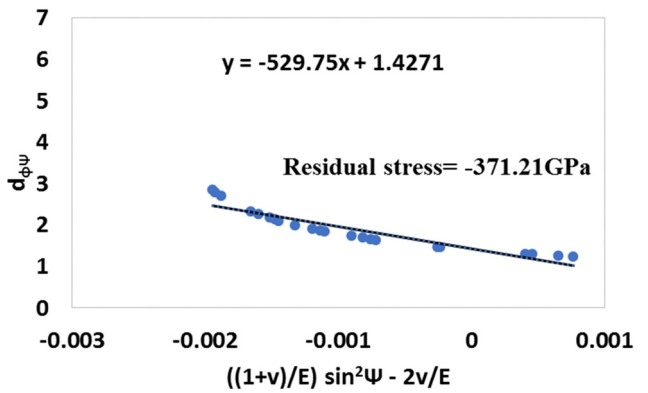

Fig. 6 Residual stress of plaster of Paris from the XRD-sin^2 Ψ technique.

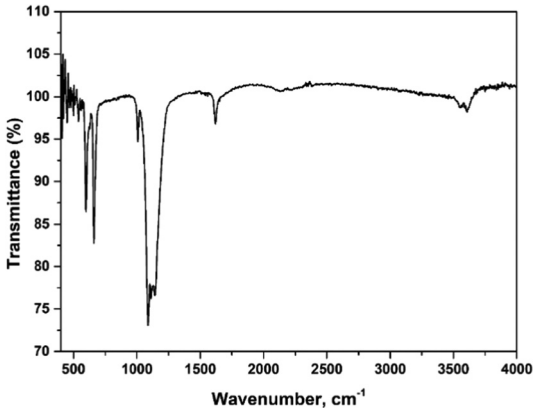

Fig. 7 FTIR of bassanite synthesized form waste eggshells.

peaks for the hydroxyl group. Similar peaks for water were reported elsewhere.[42] Three associated peaks were noticed at 1090, 1115, and 1140 cm^{-1} wavenumber, all of which appeared due to the bending vibration of the v_3 mode, with a shoulder at 990 cm^{-1} wavenumber and all of them were responsible for the presence of sulphate groups, which were compared with the literature.[43–45]

Raman spectroscopy

To characterize the synthesize sample, Raman spectroscopy was performed to identify the functional groups, and the originated spectrum is presented in Fig. 8. A very strong Raman active peak was noticed at the frequency of 1019 cm^{-1} which was attributed to the presence of sulphate groups. There were peaks in the region of 423, 485, and 615 cm^{-1} which were also responsible for the presence of sulphate groups, but these peaks were not strongly Raman active. There were water molecules present in the plaster of Paris molecule, which exerted liberation modes in the region of 400–600 cm^{-1} which coupled with the brand of sulphate in this region resulting in an overlap. A similar type of overlap was reported with a similar Raman spectrum.[46]

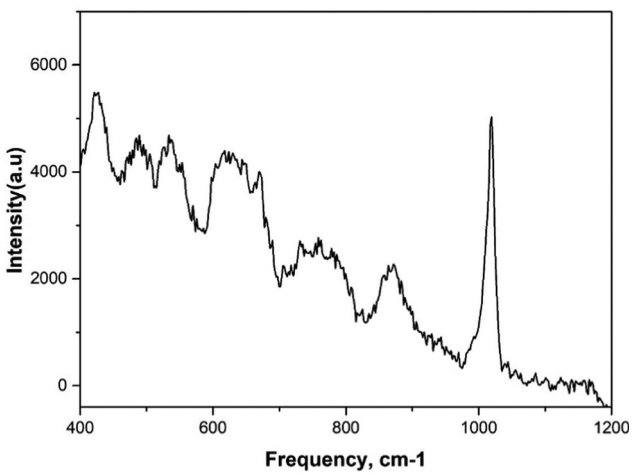

Fig. 8 Raman spectroscopy of the synthesized plaster of Paris.

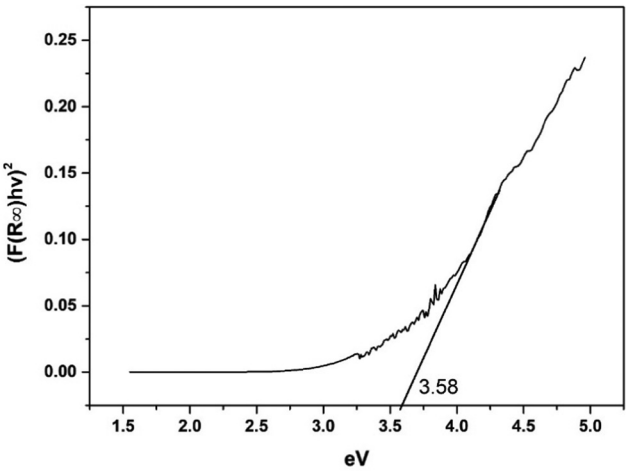

Fig. 9 Optical bandgap of the synthesized plaster of Paris.

Optical bandgap estimation

The photophysical and photochemical nature of the synthesized plaster of Paris were determined by exploration of the optical bandgap energy, the energy required to move electrons from the valence band to the conduction band. The optical bandgap of the sample was measured from the Tauc plot following eqn (22).[47,48] The optical bandgap energy can be estimated from the reflectance spectra by transforming absorbance spectra utilizing P. Kubelka and F. Munk theory, which is presented here in eqn (23).[49,50]

$$\propto h\vartheta = A(h\vartheta - E_g)^n \quad (22)$$

$$F(R_\infty) = \frac{K}{S} = \frac{(1-R_\infty)^2}{2R_\infty} \quad (23)$$

Here, h = Planck constant, ν = photon's frequency, E_g = band gap energy, A = constant, K = absorption coefficient, S = scattering coefficient, and R_∞ = reflectance at infinity.

Thus, the optical bandgap energy (3.58 eV) was computed from eqn (24) and the respective graph is presented in Fig. 9.

$$F(R_\infty)h\vartheta = A(h\vartheta - E_g)^n \quad (24)$$

Scanning electronic microscopic analysis

To explore the surface morphology of the synthesized plaster of Paris, it was was examine under scanning electronic microscopy. The image revealed that there was no uniformity among the particles under consideration but most of the particle shapes were rod shape with a few needle-like shapes. Previously, needle shape plaster of Paris was reported in a published article.[45,51] The electronic image carried good evidence that the particles of the plaster of Paris remained in aggregation form. Fig. 10 displays the electronic image of the synthesized plaster of Paris from waste eggshells.

Hemolysis assessment

Estimation of the hemolytic property is one of the most common tests of any biomaterial candidate for biomedical applications.[52] There are a number of test methods available

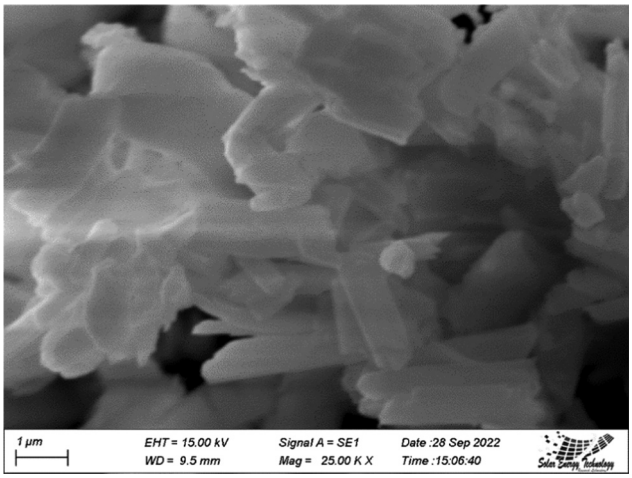

Fig. 10 SEM image of plaster of Paris.

for the estimation of the percentage of hemolysis, which is based on plasma free hemoglobin and its derivative measurement[52,53] which was followed for the case of plaster of Paris (shown in Fig. 11). The maximum percentage (4.7%) of hemolysis was noticed for the 200 μg ml^{-1} sample and the minimum (1.4%) was for the 50 μg ml^{-1} dose. These figures indicated that with the increment of the sample dose, the hemolysis percentage was increased but remained within the highly hemocompatible region. According to the ASTM data, biomaterials are characterized based on the hemolysis properties such as highly hemocompatible (<5%), hemocompatible (<10%), and non-hemocompatible (>20%).[54] The RBCs are the most abundant blood cell in the human body and responsible for various important physiological tasks. Thus, the interaction of biomaterials with RBCs is inevitable and a large fraction of biomaterials are exposed to RBCs, which determines the safe application in medical fields. The natural shape of RBCs is bio-concave type and the erythrocyte membrane is sensitive to the external environment. And the membrane is easily affected/influenced by the presence of external substances like biomaterials.[55] When the amount of the sample increased, the adsorption of the biomaterial on the RBC surface was augmented which ultimately distorted more the erythrocyte membrane and resulted in higher percentage of hemolysis. The hemolysis data presented good correlation (R^2 = 0.99, p < 0.04785).

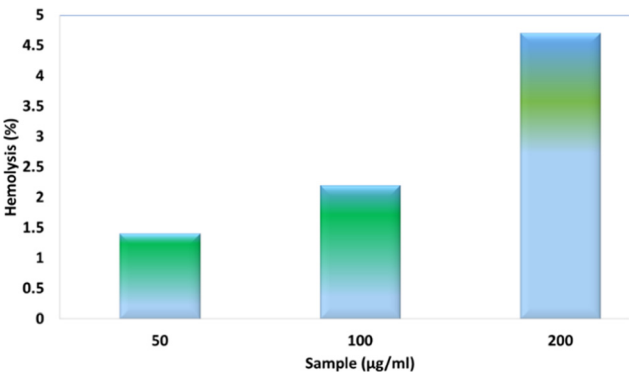

Fig. 11 Percentage haemolysis for plaster of Paris at various doses.

Cytotoxicity assessment

Cell viability and non-viability are crucial for biomaterial applications in the human body, and describe the response of cells in contact with the external biomaterials. Biomaterials are allowed on the body based on the survival, death and metabolic function of cells.[56] Fig. 12 represents the viable and non-viable cells of the control and plaster of Paris at various concentrations, which were found from an automated cell counter (LUNA-II™, Analytikjena). The control presented nearly 99% viable cells while the sample exerting 93–97% cell viability. With augmentation of the sample dose from 50 to 200 μg ml^{-1}, the percentage of cell death was enhanced. The average cell size was 8–10 μm and a variation in shape and morphology among the dead cells was visualized in the captured images. Cytoskeletal disruption may be one of the reasons for the breakdown of the cells and thus the more sample presented in the medium, the more dead cells were counted. A high residual stress (−371 GPa) in the crystals may also work as an influential factor to change the morphology of the cytoskeleton. There might be another reason for the breakdown/death of cells like mitochondrial dysfunction in toxicology by producing reactive oxygen species along with oxidative stress.[57] In the previous section, the optical bandgap was found to be 3.58 eV (~8.6 × 10^{15} Hz), which indicates that an electronic shift may have occurred in the visible range of light. This electron can cause the reduction of oxygen to form water molecules through the respiratory system. Sometimes, electrons are accepted by the oxygen molecule to form superoxide radicals or hydroxyl radicals and further peroxide, which influences the killing of cells. The more electron producing species, the more radical formation, which results in more non-viable cells. A similar type of effect was explained in a published document.[56] So, with the increment of the sample dose the percentage of non-viable cells was enhanced.

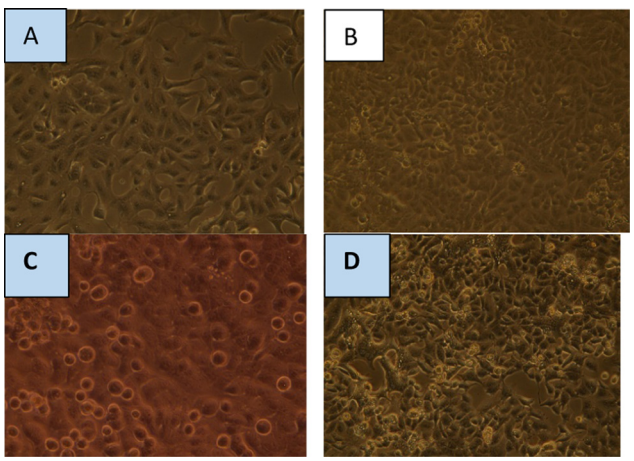

Fig. 12 Pictorial view of viable and non-viable cells after interacting with plaster of Paris: (A) control, (B) 50 μg ml^{-1}, (C) 100 μg ml^{-1}, and (D) 200 μg ml^{-1}.

E. coli S. aureus

Fig. 13 Antimicrobial property of plaster of Paris synthesized from waste eggshell.

Antimicrobial activity of the synthesized bassanite from eggshell

The antimicrobial performance of the synthesized plaster of Paris is presented here in Fig. 13 where plaster, DM and Std stand for plaster of Paris, DMSO, and standard, respectively. There was no antimicrobial effect on Gram-negative *E. coli* of the sample and thus no inhibition zone was observed. But in the case of Gram-positive *S. aureus* a larger inhibition zone was noticed, which was higher than the standard. The reason behind this variation between the Gram-negative and Gram-positive resulted from the structural difference of the cells. The cell walls of Gram-negative and Gram-positive bacteria are 20–80 nm and <10 nm, respectively, but the structural components are different.[58] The Gram-negative bacteria consists of a two membrane bilayer, widely known as the inner and outer membrane, and the space between is called the periplasm.[59] On the other hand, the cell wall compositions of Gram-positive bacteria are teichoic acids or relevant glycopolymers, polysaccharides, and proteins.[60] The teichoic acids are composed of lipoteichoic acids and wall teichoic acids which are responsible for the overall negative charge on the cell wall that contributes to the immune response, adhesion, and cell wall maintenance.[60,61] The cell wall structure of the Gram-negative bacteria is more complex and difficult for the penetration of materials, even in nano-size. Due to the presence of an outer membrane, providing extra defense, the Gram-negative bacteria are more resistant than the Gram-positive bacteria.[62] In contrast, the Gram-positive bacteria contain polysaccharides in their cell wall, which facilitate the ion transfer from outside to the inside of the cell where electrostatic force works as a driving force.[62] By entering the ions/particles inside the cell of Gram-positive bacteria, a lower molecular zone is produced which inhibits the regular mechanism of the cell and thus kills the bacteria. In this case a similar type of effect was noticed for *E. coli* and *S. aureus* as the representative Gram-negative and Gram-positive bacteria, respectively. The diameters of the inhibition zone of the standard and the plaster of Paris were 20 and 30 mm, respectively, for *S. aureus* bacteria.

Conclusion

Waste eggshells can be fruitfully utilized for the production of plaster of Paris, which was confirmed from the analysis of XRD, FTIR, Raman, UV-Vis-NIR, and SEM. The crystallite size calculated from the Scherrer equation and from various models revealed that the crystallite size of the product was within the nano-range. The favorable cytotoxicity, hemolysis and antimicrobial properties revealed that the synthesized product can be used in biomedical sectors. The synthesized product can also be a candidate for the inhibition of Gram-positive bacteria, which will minimize the post-surgical infection relevant problem. The explored crystallographic parameters will assist researchers in understanding the structure of materials, facilitating the final application. From this research it is suggested to consider waste eggshells for the synthesis of plaster of Paris where biocompatible properties are desired.

Author contributions

Md. Sahadat Hossain conceived and designed the experiment, analysed the data, wrote the original manuscript and performed the experiments. Md. Najem Uddin executed the cytotoxicity, haemolysis and antimicrobial assessment. Shirin Akter Jahan assisted in executing the sophisticated instrumental analysis. Samina Ahmed supervised the overall work and managed the funding with required facilities.

Data availability

The raw/processed data required to reproduce these findings cannot be shared at this time due to technical or time limitations.

Conflicts of interest

There are no conflicts to declare.

Acknowledgements

The authors are grateful to Bangladesh Council of Scientific and Industrial Research (BCSIR) authority for financial support through R&D project (ref. no. 39.02.0000.011.14.134.2021/900; Date: 30.12.2021). The authors also wish to thank Strengthening Institute of Glass and Ceramics Research & Testing project for sophisticated instrumental support. The authors also acknowledge the Raman spectroscopic support from the Central Analytical and Research Facilities (CARF).

References

1 H. Sharma and D. Prabu, Plaster of Paris: Past, Present and Future, *J. Clin. Orthop. Trauma*, 2013, **4**(3), 107–109.
2 J. C. Colditz, Plaster of Paris: The Forgotten Hand Splinting Material, *J. Hand Ther.*, 2002, **15**(2), 144–157.
3 P. Hernigou, Plaster of Paris: The Orthopaedic Surgeon Heritage, *Int. Orthop.*, 2016, **40**(8), 1767–1779.
4 M. Burgos-Ruiz, G. Pelayo-Punzano, E. Ruiz-Agudo, K. Elert and C. Rodriguez-Navarro, Synthesis of High Surface Area

$CaSO_4 0.5H_2O$ Nanorods Using Calcium Ethoxide as Precursor, *Chem. Commun.*, 2021, **57**(59), 7304–7307.
5 M. Zwawi, Recent Advances in Bio-Medical Implants; Mechanical Properties, Surface Modifications and Applications, *Eng. Res. Express*, 2022, **4**(3), 032003.
6 T. Nissinen, M. Li, N. Brielles and S. Mann, Calcium Sulfate Hemihydrate-Mediated Crystallization of Gypsum on Ca^{2+}-Activated Cellulose Thin Films, *CrystEngComm*, 2013, **15**(19), 3793–3798.
7 J. Borrelli, W. D. Prickett and W. M. Ricci, Treatment of Nonunions and Osseous Defects with Bone Graft and Calcium Sulfate, *Clin. Orthop. Relat. Res.*, 2003, **411**, 245–254.
8 A. S. Coetzee, Regeneration of Bone in the Presence of Calcium Sulfate, *Arch. Otolaryngol.*, 1980, **106**(7), 405–409.
9 G. H. Lee, J. G. Khoury, J.-E. Bell and J. A. Buckwalter, Adverse Reactions to Osteoset Bone Graft Substitute: The Incidence in a Consecutive Series, *Iowa Orthop. J*, 2002, **22**, 35.
10 D. Robinson, D. Alk, J. Sandbank, R. Farber and N. Halperin, Inflammatory Reactions Associated with a Calcium Sulfate Bone Substitute, *Ann. Transplant.*, 1999, **4**(3–4), 91–97.
11 O. Al Rugaie, M. S. Jabir, M. K. Mohammed, R. H. Abbas, D. S. Ahmed, G. M. Sulaiman, S. A. Mohammed, R. A. Khan, K. A. Al-Regaiey and M. Alsharidah, Modification of SWCNTs with Hybrid Materials ZnO–Ag and ZnO–Au for Enhancing Bactericidal Activity of Phagocytic Cells against Escherichia Coli through NOX2 Pathway, *Sci. Rep.*, 2022, **12**(1), 1–12.
12 Y.-W. Wang and F. C. Meldrum, Additives Stabilize Calcium Sulfate Hemihydrate (Bassanite) in Solution, *J. Mater. Chem.*, 2012, **22**(41), 22055–22062.
13 A. K. Srivastava, A. Saxena and A. R. Dixit, Investigation on the Thermal Behaviour of AZ31B/Waste Eggshell Surface Composites Produced by Friction Stir Processing, *Compos. Commun.*, 2021, **28**, 100912.
14 R. Vinayagam, S. Kandati, G. Murugesan, L. C. Goveas, A. Baliga, S. Pai, T. Varadavenkatesan, K. Kaviyarasu and R. Selvaraj, Bioinspiration Synthesis of Hydroxyapatite Nanoparticles Using Eggshells as a Calcium Source: Evaluation of Congo Red Dye Adsorption Potential, *J. Mater. Res. Technol*, 2022, **22**, 169–180.
15 M. A. Hussein, M. A. Azeem, A. M. Kumar and N. M. Emara, Processing and in Vitro Corrosion Analysis of Sustainable and Economical Eggshell Reinforced Mg and Mg-Zr Matrix Composite for Biomedical Applications, *Mater. Today Commun.*, 2022, **32**, 103944.
16 T. S. Kumar, K. Madhumathi and R. Jayasree, Eggshell Waste: A Gold Mine for Sustainable Bioceramics, *J. Indian Inst. Sci.*, 2022, 1–22.
17 V. P. Padmanabhan, T. S. N. Sankara Narayanan, S. Sagadevan, M. E. Hoque and R. Kulandaivelu, Advanced Lithium Substituted Hydroxyapatite Nanoparticles for Antimicrobial and Hemolytic Studies, *New J. Chem.*, 2019, **43**(47), 18484–18494.
18 M. F. Ilker, K. Nüsslein, G. N. Tew and E. B. Coughlin, Tuning the Hemolytic and Antibacterial Activities of Amphiphilic Polynorbornene Derivatives, *J. Am. Chem. Soc.*, 2004, **126**(48), 15870–15875.
19 M. E. Fait, M. Hermet, F. Comelles, P. Clapés, H. A. Alvarez, E. Prieto, V. Herlax, S. R. Morcelle and L. Bakás, Microvesicle Release and Micellar Attack as the Alternative Mechanisms Involved in the Red-Blood-Cell-Membrane Solubilization Induced by Arginine-Based Surfactants, *RSC Adv.*, 2017, **7**(60), 37549–37558.
20 Z. S. Abbas, G. M. Sulaiman, M. S. Jabir, S. A. Mohammed, R. A. Khan, H. A. Mohammed and A. Al-Subaiyel, Galangin/β-Cyclodextrin Inclusion Complex as a Drug-Delivery System for Improved Solubility and Biocompatibility in Breast Cancer Treatment, *Molecules*, 2022, **27**(14), 4521.
21 S. Sultana, M. S. Hossain, M. Mahmud, M. B. Mobarak, M. H. Kabir, N. Sharmin and S. Ahmed, UV-Assisted Synthesis of Hydroxyapatite from Eggshells at Ambient Temperature: Cytotoxicity, Drug Delivery and Bioactivity, *RSC Adv.*, 2021, **11**(6), 3686–3694.
22 S. Stagnoli, M. A. Luna, C. C. Villa, F. Alustiza, A. Niebylski, F. Moyano, N. M. Correa and R. D. Falcone, Unique Catanionic Vesicles as a Potential ''Nano-Taxi'' for Drug Delivery Systems. In Vitro and in Vivo Biocompatibility Evaluation, *RSC Adv.*, 2017, **7**(9), 5372–5380, DOI: **10.1039/C6RA27020D**.
23 S. J. Bakht Dalir, H. Djahaniani, F. Nabati and M. Hekmati, Characterization and the Evaluation of Antimicrobial Activities of Silver Nanoparticles Biosynthesized from Carya Illinoinensis Leaf Extract, *Heliyon*, 2020, **6**(3), e03624.
24 A. Rautela and J. Rani, Green Synthesis of Silver Nanoparticles from Tectona Grandis Seeds Extract: Characterization and Mechanism of Antimicrobial Action on Different Microorganisms, *J. Anal. Sci. Technol.*, 2019, **10**(1), 1–10.
25 K. Mishima, Y. T. Okabe, M. Mizuno, K. Ohno, H. Kitoh and S. Imagama, Efficacy of Soluble Lansoprazole-Impregnated Beta-Tricalcium Phosphate for Bone Regeneration, *Sci. Rep.*, 2022, **12**(1), 1–10.
26 Md. S. Hossain, Md. N. Uddin, S. Sarkar and S. Ahmed, Crystallographic Dependency of Waste Cow Bone, Hydroxyapatite, and β-Tricalcium Phosphate for Biomedical Application, *J. Saudi Chem. Soc.*, 2022, **26**(6), 101559, DOI: **10.1016/j.jscs.2022.101559**.
27 S. Fukugaichi and N. Matsue, One-Step Synthesis of Calcium Sulfate Hemihydrate Nanofibers from Calcite at Room Temperature, *ACS Omega*, 2018, **3**(3), 2820–2824.
28 M. S. Hossain, M. A. A. Shaikh, M. S. Rahaman and S. Ahmed, Modification of the Crystallographic Parameters in a Biomaterial Employing a Series of Gamma Radiation Doses, *Mol. Syst. Des. Eng.*, 2022, **7**, 1239–1248, DOI: **10.1039/D2ME00061J**.
29 Y. Yoon, K. Katsumata, S. Park, A. Fujishima and J. Hong, Enhanced Hydrogen Production at Optimum PH for the Recovery Cycle of β-FeOOH, *ACS Omega*, 2022, **7**(18), 16049–16054.
30 A. Das and P. Dobbidi, Impedance Spectroscopy and Ac Conductivity in $Ba_{0.5}Sr_{0.5}TiO_3$–$Ca_{10}(PO_4)_6(OH)_2$ Ceramic Composites: An Electrical Approach to Unveil Biocomposites, *ACS Biomater. Sci. Eng.*, 2021, **7**(6), 2296–2308.

31 M. Sharma, R. Nagar, V. K. Meena and S. Singh, Electro-Deposition of Bactericidal and Corrosion-Resistant Hydroxyapatite Nanoslabs, *RSC Adv.*, 2019, **9**(20), 11170–11178.

32 M. S. Hossain and S. Ahmed, Synthesis of Nano-Crystallite Gypsum and Bassanite from Waste Pila Globosa Shells: Crystallographic Characterization, *RSC Adv.*, 2022, **12**(38), 25096–25105.

33 K. V. Kumar, T. J. Subha, K. G. Ahila, B. Ravindran, S. W. Chang, A. H. Mahmoud, O. B. Mohammed and M. A. Rathi, Spectral Characterization of Hydroxyapatite Extracted from Black Sumatra and Fighting Cock Bone Samples: A Comparative Analysis, *Saudi J. Biol. Sci.*, 2021, **28**(1), 840–846.

34 Md. S. Hossain, M. Mahmud, M. B. Mobarak, S. Sultana, Md. A. A. Shaikh and S. Ahmed, New Analytical Models for Precise Calculation of Crystallite Size: Application to Synthetic Hydroxyapatite and Natural Eggshell Crystalline Materials, *Chem. Pap.*, 2022, **76**, 7245–7251, DOI: **10.1007/s11696-022-02377-9**.

35 M. Hossain, M. Mahmud, M. B. Mobarak and S. Ahmed, Crystallographic Analysis of Biphasic Hydroxyapatite Synthesized by Different Methods: An Appraisal between New and Existing Models, *Chem. Pap.*, 2022, **76**(3), 1593–1605.

36 S. L. Mousavi, F. Jamali-Sheini, M. Sabaeian and R. Yousefi, Correlation of Physical Features and the Photovoltaic Performance of P3HT: PCBM Solar Cells by Cu-Doped SnS Nanoparticles, *J. Phys. Chem. C*, 2021, **125**(29), 15841–15852.

37 M. S. Hossain, S. M. Tuntun, N. M. Bahadur and S. Ahmed, Enhancement of Photocatalytic Efficacy by Exploiting Copper Doping in Nano-Hydroxyapatite for Degradation of Congo Red Dye, *RSC Adv.*, 2022, **12**(52), 34080–34094.

38 S. Marola, S. Bosia, A. Veltro, G. Fiore, D. Manfredi, M. Lombardi, G. Amato, M. Baricco and L. Battezzati, Residual Stresses in Additively Manufactured AlSi10Mg: Raman Spectroscopy and X-Ray Diffraction Analysis, *Mater. Des.*, 2021, **202**, 109550.

39 J. Sanahuja, L. Dormieux, S. Meille, C. Hellmich and A. Fritsch, Micromechanical Explanation of Elasticity and Strength of Gypsum: From Elongated Anisotropic Crystals to Isotropic Porous Polycrystals, *J. Eng. Mech. Div., Am. Soc. Civ. Eng.*, 2010, **136**(2), 239–253.

40 J. Fu, Elastic Constants and Homogenized Moduli of Monoclinic Structures Based on Density Functional Theory, *Density Functional Calculations: Recent Progresses of Theory and Application*, 2018, vol. 219.

41 W. M. Schwerdtner, J.-M. Tou and P. B. Hertz, Elastic Properties of Single Crystals of Anhydrite, *Can. J. Earth Sci.*, 1965, **2**(6), 673–683.

42 J. Bensted and S. Prakash, Investigation of the Calcium Sulphate-Water System by Infrared Spectroscopy, *Nature*, 1968, **219**(5149), 60–61.

43 P. Roonasi and A. Holmgren, An ATR-FTIR Study of Sulphate Sorption on Magnetite; Rate of Adsorption, Surface Speciation, and Effect of Calcium Ions, *J. Colloid Interface Sci.*, 2009, **333**(1), 27–32.

44 P. S. R. Prasad, V. K. Chaitanya, K. S. Prasad and D. N. Rao, Direct Formation of the γ-$CaSO_4$ Phase in Dehydration Process of Gypsum: In Situ FTIR Study, *Am. Mineral.*, 2005, **90**(4), 672–678.

45 M. G. Pillai, Thin Layer Drying Kinetics, Characteristics and Modeling of Plaster of Paris, *Chem. Eng. Res. Des.*, 2013, **91**(6), 1018–1027.

46 B. J. Berenblut, P. Dawson and G. R. Wilkinson, A Comparison of the Raman Spectra of Anhydrite ($CaSO_4$) and Gypsum ($CaSO_4$)·$2H_2O$, *Spectrochim. Acta, Part A*, 1973, **29**(1), 29–36.

47 S. K. Suram, P. F. Newhouse and J. M. Gregoire, High Throughput Light Absorber Discovery, Part 1: An Algorithm for Automated Tauc Analysis, *ACS Comb. Sci.*, 2016, **18**(11), 673–681.

48 M. Nazim, A. A. P. Khan, A. M. Asiri and J. H. Kim, Exploring Rapid Photocatalytic Degradation of Organic Pollutants with Porous CuO Nanosheets: Synthesis, Dye Removal, and Kinetic Studies at Room Temperature, *ACS Omega*, 2021, **6**(4), 2601–2612.

49 P. Kubelka and F. Munk, An Article on Optics of Paint Layers, *Z. Tech. Phys.*, 1931, **12**(593–601), 259–274.

50 P. Maku\la, M. Pacia and W. Macyk, How to Correctly Determine the Band Gap Energy of Modified Semiconductor Photocatalysts Based on UV–Vis Spectra, *J. Phys. Chem. Lett.*, 2018, **9**, 6814–6817.

51 J. J. Eberl and A. R. Ingram, Process for Making High-Strength Plaster of Paris, *Ind. Eng. Chem.*, 1949, **41**(5), 1061–1065.

52 M. A. Dobrovolskaia, J. D. Clogston, B. W. Neun, J. B. Hall, A. K. Patri and S. E. McNeil, Method for Analysis of Nanoparticle Hemolytic Properties in Vitro, *Nano Lett.*, 2008, **8**(8), 2180–2187.

53 C. Chouly, L. Bordenave, R. Bareille, V. Guerin, A. Baquey, D. Pouliquen, C. H. Baquey and P. Jallet, In Vitro Study of the Hemocompatibility of Superparamagnetic Contrast Agent for Magnetic Resonance Imaging, *Clin. Mater.*, 1994, **15**(4), 293–301.

54 V. S. Chandra, K. Elayaraja, K. T. Arul, S. Ferraris, S. Spriano, M. Ferraris, K. Asokan and S. N. Kalkura, Synthesis of Magnetic Hydroxyapatite by Hydrothermal–Microwave Technique: Dielectric, Protein Adsorption, Blood Compatibility and Drug Release Studies, *Ceram. Int.*, 2015, **41**(10), 13153–13163.

55 J. Lin, L. Huang, H. Ou, A. Chen, R. Xiang and Z. Liu, Effects of ZIF-8 MOFs on Structure and Function of Blood Components, *RSC Adv.*, 2021, **11**(35), 21414–21425.

56 P. V. AshaRani, G. Low Kah Mun, M. P. Hande and S. Valiyaveettil, Cytotoxicity and Genotoxicity of Silver Nanoparticles in Human Cells, *ACS Nano*, 2009, **3**(2), 279–290.

57 T. Xia, M. Kovochich, J. Brant, M. Hotze, J. Sempf, T. Oberley, C. Sioutas, J. I. Yeh, M. R. Wiesner and A. E. Nel, Comparison of the Abilities of Ambient and Manufactured Nanoparticles to Induce Cellular Toxicity According to an Oxidative Stress Paradigm, *Nano Lett.*, 2006, **6**(8), 1794–1807.

58 A. Mai-Prochnow, M. Clauson, J. Hong and A. B. Murphy, Gram-positive and Gram-negative Bacteria Differ in Their Sensitivity to Cold Plasma, *Sci. Rep.*, 2016, **6**(1), 1–11.
59 S. I. Miller and N. R. Salama, The Gram-negative Bacterial Periplasm: Size Matters, *PLoS Biol.*, 2018, **16**(1), e2004935.
60 L. G. Harris, Microbial Cell Structure and Organization: Bacteria, *J. Encycl. Infect. Immun.*, 2022, 345–362.
61 J.-F. Xia, X.-M. Zhao and D.-S. Huang, Predicting Protein–Protein Interactions from Protein Sequences Using Meta Predictor, *Amino Acids*, 2010, **39**(5), 1595–1599.
62 S. J. Lam, N. M. O'Brien-Simpson, N. Pantarat, A. Sulistio, E. H. Wong, Y.-Y. Chen, J. C. Lenzo, J. A. Holden, A. Blencowe and E. C. Reynolds, Combating Multidrug-Resistant Gram-negative Bacteria with Structurally Nanoengineered Antimicrobial Peptide Polymers, *Nat. Microbiol.*, 2016, **1**(11), 1–11.